Chinese Chemical Letters 37 (2026) 111536

Contents lists available at ScienceDirect

Chinese Chemical Letters

journal homepage: www.elsevier.com/locate/cclet

High-throughput screening of high C/N-ratio homonuclear dual-atom catalysts for electrochemical reduction of nitrate to ammonia

Yahui Li[a], Quanchen Feng[a], Krisztina László[b], Ying Wang[a,*]

[a] State Key Laboratory of Water Pollution Control and Green Resource Recycling, Shanghai Institute of Pollution Control and Ecological Security, School of Environmental Science and Engineering, Tongji University, Shanghai 200092, China
[b] Department of Physical Chemistry and Materials Science, Faculty of Chemical Technology and Biotechnology, Budapest University of Technology and Economics, Budapest 1111, Hungary

ARTICLE INFO

Article history:
Received 21 December 2024
Revised 30 April 2025
Accepted 2 July 2025
Available online 3 July 2025

Keyword:
Homonuclear dual-atom catalysts
Electrocatalysis
Nitrate reduction reaction
Hydrogen evolution reaction
Density functional theory

ABSTRACT

To deal with the problem of NO_3^- enrichment in water environment, electrochemical catalysis of nitrate reduction reaction (NO_3RR) provides a possibility. However, this catalytic process requires efficient and highly selective NO_3RR electrocatalysts to catalyze NO_3^- conversion. Consequently, the objective of this work is to search highly active NO_3RR electrocatalysts by employing an efficient screening strategy using density functional theory methods. The catalytic activity is assessed by calculating limiting potential $U_L(NO_3RR)$ and $U_L(HER)$. The research results indicate that $Os_2_C_{19}N_3$ not only has excellent catalytic activity ($U_L(NO_3RR) = -0.15$ V), but also can effectively avoid the occurrence of competitive hydrogen evolution reaction. The NO_3RR process of $Os_2_C_{19}N_3$ is $^* + NO_3^- \rightarrow {}^*NO_3 \rightarrow {}^*NO_3H \rightarrow NO_2 \rightarrow {}^*NO_2H \rightarrow {}^*NO \rightarrow {}^*NOH \rightarrow {}^*N \rightarrow {}^*NH \rightarrow {}^*NH_2 \rightarrow {}^*NH_3 \rightarrow {}^* + NH_3$. When $Os_2_C_{19}N_3$ is in the condition of DFT-Sol, DFT-D, and DFT-D-Sol, the NO_3RR process is $^* + NO_3^- \rightarrow {}^*NO_3 \rightarrow {}^*NO_3H \rightarrow NO_2 \rightarrow {}^*NO_2H \rightarrow {}^*NO \rightarrow {}^*NOH \rightarrow {}^*NHOH \rightarrow {}^*NH_2OH \rightarrow {}^*NH_2 \rightarrow {}^*NH_3 \rightarrow {}^* + NH_3$, and the $U_L(NO_3RR)$ values are −0.06, −0.15, and −0.06 V, respectively. This research may offer potential reference values for the development of innovative NO_3RR catalysts and the synthesis of NH_3.

© 2025 Published by Elsevier B.V. on behalf of Chinese Chemical Society and Institute of Materia Medica, Chinese Academy of Medical Sciences.

Although the excessive consumption of fossil energy has brought great development of society and technology, it has also led to new environmental problems and energy crisis [1,2]. Especially in the context of carbon peak and carbon neutrality, the use of clean energy sources to replace fossil energy sources is extremely significant [3,4]. Researchers have conducted extensive studies on energy sources, such as superoxide generated amines [5] and catalytic oxidation of sulfides [6]. As one of the important renewable carbon-free energy carrier, ammonia (NH_3) is environmentally friendly, low cost, high safety, and the heat loss ratio of ammonia combustion is much lower than that of gasoline and hydrogen, which makes it have a good potential for ammonia energy development [7,8]. At present, the industrial production of NH_3 mainly relies on the Haber-Bosch process, which not only has high conditions for temperature and pressure, but also produces a large amount of carbon dioxide [9,10]. Therefore, it is of great significance to explore the efficient green way of NH_3 production for achieving carbon peak and carbon neutrality.

In search of an effective alternative solution to ammonia production by the Haber-Bosch process, the electrochemical N_2 reduction reaction (NRR) and nitrate reduction reaction (NO_3RR) have attracted considerable research interest in the past few years due to its lower energy consumption and lower CO_2 emissions [11,12]. However, the high dissociation energy of N≡N bond leads to the problems of poor yield and low selectivity [13]. The dissociation energy of the N=O bond for NO_3^- (204 kJ/mol) is much lower than that of the N≡N bond (941 kJ/mol) [14], which lays a solid foundation for improving NH_3 formation kinetics. In addition, electroreduction of NO_3^- can also effectively mitigate the problem of NO_3^- enrichment in water environment, so that other pollutants can be effectively removed by the addition of synthetic cleaning chemical [15,16]. Therefore, electrochemical catalytic NO_3RR provide new opportunities for large-scale production of NH_3 under environmental conditions [17,18], which is of great significance for achieving carbon peak and carbon neutrality [19,20]. Finding efficient and highly selective NO_3RR electrocatalysts is the key to catalyze NO_3^- conversion.

In recent years, two-dimensional carbon-nitride materials (*e.g.*, C_2N, C_3N_4, and C_4N) have been widely studied and proved to be the excellent transition metal doped substrates in the field of elec-

* Corresponding author.
E-mail address: yingwang@tongji.edu.cn (Y. Wang).

https://doi.org/10.1016/j.cclet.2025.111536
1001-8417/© 2025 Published by Elsevier B.V. on behalf of Chinese Chemical Society and Institute of Materia Medica, Chinese Academy of Medical Sciences.

trocatalysis [21-23]. Transition metal doped often forms M – N coordination centers, which have been shown to catalyze oxygen reduction reaction, oxygen evolution reaction, NRR, and NO_3RR [24,25]. Zhu *et al.* have proved that Hf/g-C_2N are predicted as potential electrocatalysts for the NO_3RR with limiting potential (U_L) values of −0.27 V [26]. Lv *et al.* have been explored that Ru/g-C_3N_4 is the most promising catalysts because of its lowest energy barrier and extraordinary selectivity [27]. The nuclear number of transition metal active centers can significantly regulate the catalytic activity of the catalyst. That is, different from single-atom catalysts, dual-atom catalysts (DACs) can provide more active sites and active configurational space, and the synergistic effect of dual transition metal atoms can effectively regulate the catalytic activity [28-30]. For example, Lv *et al.* have used DFT methods to calculate NO_3RR catalytic activity for transition-metal dimer embedded N-doped graphene [16]. The calculated results have shown that under the synergistic action of dual transition metal atoms, Cu_2@NG exhibits the lowest U_L of −0.36 V. Wu *et al.* have efficiently screened dual-atom Fe_2 DAC anchored by N-doped porous graphene (Fe_2@NG) for producing NH_3, which exhibits a rather low $U_L = -0.45$ V [31]. In addition, Chen *et al.* have designed novel homonuclear transition metals supported on N-doped graphene (TM_2/N_6-G). Cr_2/N_6-G, Mn_2/N_6-G, and Cu_2/N_6-G have demonstrated that they possess the excellent NH_3 conversion and the Faradic efficiency are greater than 61.28 %, which makes them serve as the promising NO_3RR catalysts [32]. Shen *et al.* have indicated that double atom doped g-C_3N_4 can find efficient NO_3RR catalysts [33]. Recently, Tan *et al.* have proposed four novel carbon-nitride materials (C_7N_3, $C_{10}N_3$, $C_{13}N_3$, and $C_{19}N_3$) and demonstrated that they have excellent electrical conductivity, which makes them possess excellent potential in the field of electrocatalysis [34]. Transition metal doped them can form M-N active center, which provides the basic guarantee for catalyzing NO_3RR. However, current studies have shown that they have the potential to catalyze ORR and OER [35]. For example, Cai *et al.* have demonstrated by DFT that C_7N_3 is a good substrate to load transition metal, forming a catalyst that can effectively catalyze ORR [36]. Moreover, Chen *et al.* have proven that Rh-$C_{13}N_3$ possesses the lowest overpotentials and exhibits superior ORR and OER bifunctional catalytic activity [35]. The outstanding performance of these materials in ORR and OER raises high expectations for their potential in NO_3RR. Therefore, based on the above analysis, we speculate that transition metal doped C_7N_3, $C_{10}N_3$, $C_{13}N_3$, and $C_{19}N_3$ may exhibit good catalytic potential for NO_3RR.

In this work, we systematically investigated the possibility of homonuclear dual transition metal atoms doped C_7N_3, $C_{10}N_3$, $C_{13}N_3$, and $C_{19}N_3$ (M_2-C_xN_3) as NO_3RR catalysts by DFT methods. The homonuclear dual-atom is doped into the pore of carbon-nitride material to form the M-N_x active center with the surrounding N atoms. Firstly, the stability of M_2-C_xN_3 was evaluated by calculating formation energy (E_f) and dissolution potential (U_{diss}). The density of states (DOS) and band structures are calculated to describe the electronic properties of the catalyst. Secondly, the adsorption behaviors of NO_3^-, $U_L(NO_3RR)$ and the free energy diagrams are calculated to evaluate the NO_3RR catalytic performance. In particular, the solvation effects and dispersion correction on catalytic activity were also considered of M_2-C_xN_3 with excellent NO_3RR catalytic performance. Thirdly, the competitive reaction of hydrogen evolution reaction (HER) on M_2-C_xN_3 was studied. Then, the electronic structure analysis of Os_2-$C_{19}N_3$ were conducted. Finally, the first-principles molecular dynamics (FPMD) calculation of Os_2-$C_{19}N_3$ was calculated at 300 and 500 K to further evaluate stability. This work can not only effectively predict and high-throughput screening NO_3RR electrocatalysts with high performance, but also provide effective guidance value for experiments.

The spin-unrestricted DFT framework and implemented with the DMol^3 module was used in the Materials Studio software [37,38]. The Perdew-Burke-Ernzerhof (PBE) functional of generalized gradient approximation (GGA) was employed as the exchange and correlation model [39]. The atomic orbitals' basic set was described using a double numerical plus polarization (DNP) method [40]. Convergence criteria were set as follows: energy convergence of 2×10^{-5} Ha, maximum force convergence of 0.004 Ha/Å, and maximum displacement convergence of 0.005 Å. To avoid artificial interactions, a vacuum layer with a thickness of 30 Å was used. For optimization, a $3 \times 3 \times 1$ k-point grid centered around Γ was used, while electronic structure calculations (DOS, Mulliken charge, and deformation charge density) employed a dense $5 \times 5 \times 1$ k-point grid. The FPMD calculations are performed during a period of 2 ps at the temperatures of 300 and 500 K.

The catalyst's stability was assessed in detail using E_f and U_{diss} [41,42]. E_f mainly focuses on exploring the change of per dopant atom to the stability of the catalyst. The calculation formulas for these parameters are provided below:

$$E_f = (E_{total} - E_{substrate} - 2E_{TM})/2 \quad (1)$$

$$U_{diss} = U^o{}_{diss}(\text{metal, bulk}) - E_f/ne \quad (2)$$

where, the E_{total}, $E_{substrate}$, and E_{TM} correspond to the total energy of the catalyst, the substrate, and the energy of transition metal atoms in their bulk structure, respectively. $U^o{}_{diss}$(metal, bulk) denotes the standard dissolution potential of the bulk metal, while n signifies the number of electrons participating in the dissolution process.

In this study, the reaction processes between NO_3RR and intermediates were understood through the framework of thermodynamics. The equation of the whole reaction pathway from NO_3RR to NH_3 is as follows [43]:

$$NO_3^- + 9H^+ + 8e^- \rightarrow NH_3 + 3H_2O \quad (3)$$

The Gibbs free energy change (ΔG) of each elementary step during NO_3RR process was computed by the widely employed computational hydrogen electrode (CHE) model [44,45]:

$$\Delta G = \Delta E + \Delta ZPE - T\Delta S \quad (4)$$

where, E, T, ΔZPE, and ΔS represents the total energy, the temperature of 298.15 K, the change of zero-point energy, and the difference of the entropy, respectively.

The adsorption energy (E_{ads}) is calculated as follows [46]:

$$E_{ads} = E_{*species} - E_* - E_{species} \quad (5)$$

where, the $E_{*species}$, E_*, and $E_{species}$ are the energies of species adsorbed on catalyst, catalyst, and species, respectively.

For the adsorption free energy of $^*NO_3$ (ΔG_{*NO_3}), the calculation formula is as follows [47]:

$$\Delta G_{*NO_3} = G_{*NO_3} - G_* - G_{HNO_3(g)} + 1/2G_{H_2(g)} \quad (6)$$

where, G_{*NO_3}, G_*, $G_{HNO_3(g)}$, and $G_{H_2(g)}$ are the Gibbs free energy of NO_3^- adsorbed on catalyst, catalyst, HNO_3, and H_2 molecules, respectively.

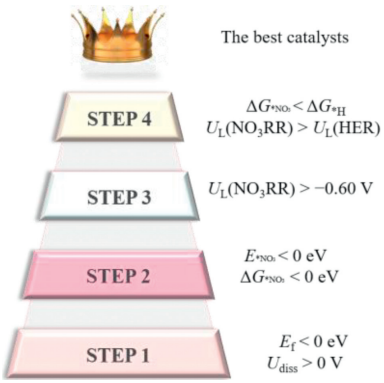
Since the energy of HNO_3 used in the above formula is gaseous energy, it is necessary to correct the formula. The correction formula is as follows:

$$\Delta G_{*NO_3-correct} = G_{*NO_3} - G_* - G_{HNO_3(g)} + 1/2G_{H_2(g)} + \Delta G_{correct} \quad (7)$$

where, $\Delta G_{correct}$ is the correction of free ion energy, and the value is 0.392 eV according to previous studies [47].

The theoretical limiting potential (U_L) can be defined as [48]:

$$U_L = -\Delta G_{max}/e \quad (8)$$



Scheme 1. Screening process for NO_3RR electrocatalyst.

The hydrogen adsorption energy (ΔE_{*H}) is represented by the equation:

$$\Delta E_{*H} = E_{*H} + E_* - 1/2E_{H_2} \quad (9)$$

where, E_{*H}, E_*, and E_{H_2} are the total energies the total energies of catalyst adsorpted with H atom, catalyst, and H_2 molecule, respectively.

The ΔG_{*H} can assess the HER catalytic activity and the formula is as follows [49]:

$$\Delta G_{*H} = \Delta E_{*H} + \Delta ZPE - T\Delta S \quad (10)$$

The main purpose of this work is to search for highly active NO_3RR electrocatalysts through efficient screening methods. Therefore, a strategy with four filtering steps is designed, as shown in Scheme 1. For this screening strategy, structural stability is first evaluated by calculating E_f and U_{diss}. After screening catalysts with excellent stability, the adsorption behaviors of NO_3^- is calculated on all catalysts, which is a prerequisite step for NO_3RR. Then, the electrocatalysts with excellent NO_3RR are found by calculating $U_L(NO_3RR)$. Finally, a good electrocatalyst must be able to withstand the competitive impact of HER. If the candidate satisfies both $\Delta G_{*NO_3} < \Delta G_{*H}$ and $U_L(NO_3RR) > U_L(HER)$, it has great potential to catalyze NO_3RR.

In this work, the crystal structure can be made by graphene supermonomers by removing the C atom of the six-membered ring and replacing the N atom. All substrates (C_7N_3, $C_{10}N_3$, $C_{13}N_3$, and $C_{19}N_3$) are constructed and presented in Fig. 1a and Figs. S1a-c (Supporting information). All transition metals considered in this work are shown in Fig. S1d (Supporting information). Meanwhile, the dual transition metal atom doped with the surrounding N atoms can form two coordination structures, one for M_2N_4 active center, named M_2-C_xN_3-I, and one for M_2N_6 active center, named M_2-C_xN_3-II, as shown in Figs. 1b and c and Fig. S2 (Supporting information).

In order to evaluate whether the electrocatalyst has excellent thermodynamic and electrochemical stability in the catalytic NO_3RR process, E_f and U_{diss} are respectively calculated as parameters for evaluating thermodynamic and electrochemical stability [46], and the results are presented in Figs. 1d and e and Fig. S3 (Supporting information). When E_f is less than 0 eV, it indicates that the M_2-C_xN_3-I and M_2-C_xN_3-II have the good thermodynamic stability. When U_{diss} is greater than 0 V, it indicates that the M_2-C_xN_3-I and M_2-C_xN_3-II have the good electrochemical stability. The greater the absolute value of E_f and U_{diss}, the more stable the catalyst. For the calculated results, it can be observed that most of the M_2-C_xN_3-I and M_2-C_xN_3-II have good stability. In particular, the E_f values of Zn-C_xN_3 can reach −3 eV or even more negative. In addition, taking Ni doped as an example, it can be observed that all Ni_2-C_xN_3 have excellent thermodynamic and electrochemical stability. However, the stability of catalyst is different for different doping configurations. For example, the E_f values of Ni_2-C_7N_3-I and Ni_2-C_7N_3-II are −1.16 and −1.28 eV. The U_{diss} values of Ni_2-C_7N_3-I and Ni_2-C_7N_3-II are respectively 0.32 and 0.38 V. Obviously, for Ni_2-C_7N_3, the catalyst is more inclined to form Ni_2-C_7N_3-II than Ni_2-C_7N_3-I. A similar situation is found in all catalysts. Thus, in the subsequent studies, only the most stable configuration is used and defined as M_2-C_xN_3.

To have a deeper understanding of the interaction between the doped active metal and the surrounding N atoms, taking Os_2-C_xN_3 as an example, the density of state (DOS) is calculated and shown in Figs. S3a-d. It can be clearly observed that the d orbital of Os atoms overlapped significantly with the p orbital of N atoms at the Fermi level near the energy of 0 eV. In other words, there is a strong orbital hybridization between the d orbital of Os atoms

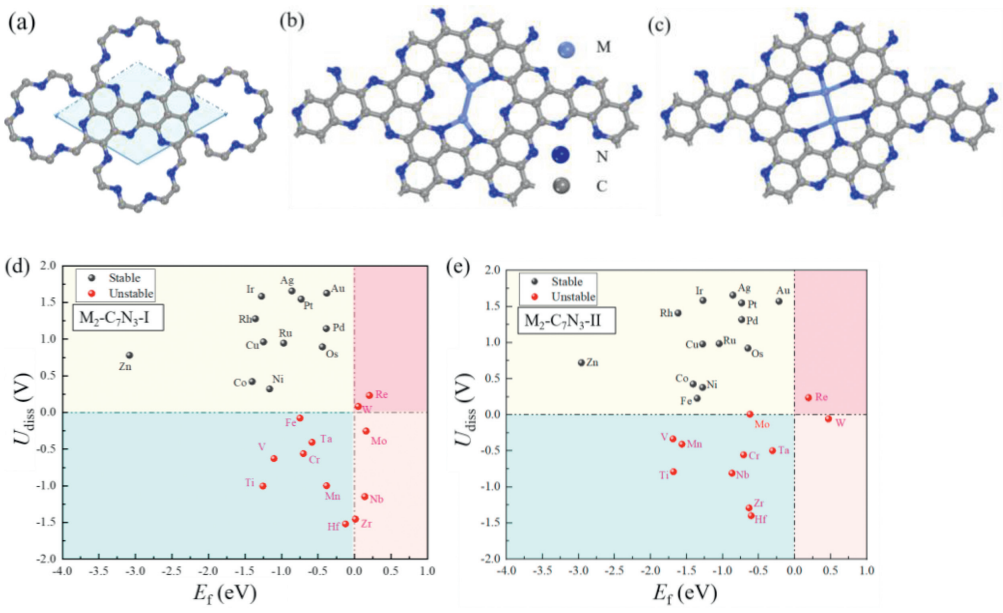


Fig. 1. Structural diagram of (a) C_7N_3, (b) M_2-C_7N_3-I and (c) M_2-C_7N_3-II. E_f and U_{diss} values of (d) M_2-C_7N_3-I and (e) M_2-C_7N_3-II.

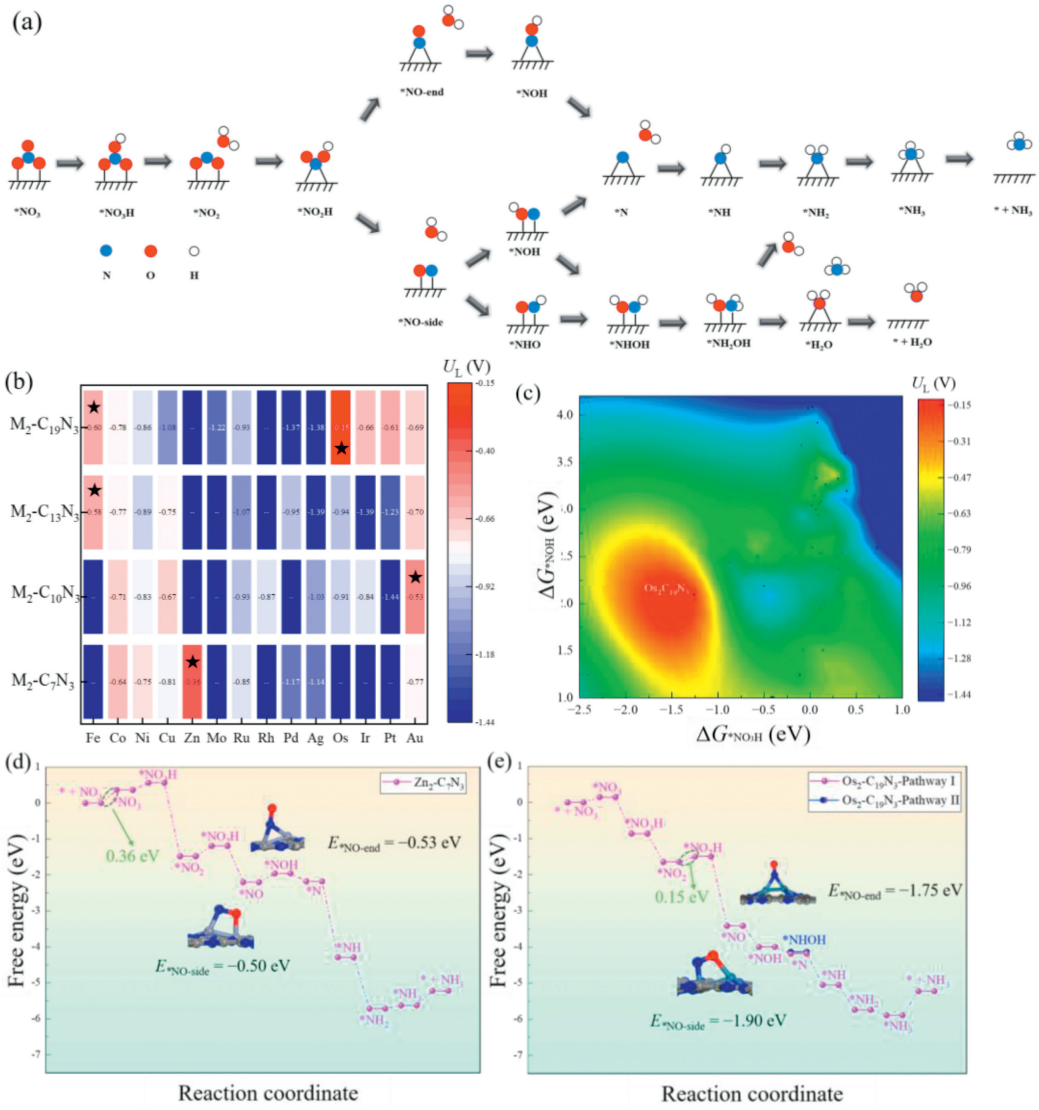


Fig. 2. (a) The considered reaction pathways of NO_3RR. (b) The limiting potentials of NO_3RR on all screening catalysts. (c) NO_3RR volcano plot of M_2-C_xN_3. Free energy diagrams for NO_3RR on (d) Zn_2-C_7N_3 and (e) Os_2-$C_{19}N_3$.

and the p orbital of N atoms, which makes Os and N atoms have a strong interaction, which provides a good basis for the stability of the Os_2-C_xN_3. In addition, M_2-C_xN_3 electrocatalytic NO_3RR requires excellent electrical conductivity. Thus, the band structures of Os_2-C_xN_3 are calculated and plotted in Figs. S3e-h. They all have extremely low band gap ($E_{band\ gap}$), which indicates that they all have very good electrical conductivity. In other words, the catalyst with lower $E_{band\ gap}$ value is advantageous for catalyzing the NO_3RR process.

In this work, the reaction considered is detailed in formula 3, involving the transfer of nine protons and eight electrons. The considered reaction pathways are shown in Fig. 2a. For these pathways, the difference mainly lies in the adsorption behavior of *NO on all stable catalyst. If the catalyst is adsorbed with *NO-end, it will likely move in the direction of removing the H_2O. If the catalyst is adsorbed with *NO-side, there are two adsorption configurations for its next hydrogenation, as shown in Fig. 2a. Firstly, the adsorption of NO_3^- is the first step, and its adsorption behavior on the catalyst is crucial for the subsequent reaction. By comparing the adsorption behavior of $*NO_3$ in various catalysts, the relative affinity of each catalyst for $*NO_3$ was predicted, and the catalytic potential of the catalyst for NO_3RR was preliminarily predicted. There are respectively two adsorption configurations for NO_3^-, that is, 1O- and 2O-manner in Fig. S5 (Supporting information). Therefore, we calculated the optimal adsorption configuration of each catalyst. The optimal adsorption energy (E_{*NO_3}) and free adsorption energy of $*NO_3$ (ΔG_{*NO_3}) are calculated and shown in Fig. S6 (Supporting information). The more negative the E_{*NO_3} and ΔG_{*NO_3}, the more inclined the reaction species to adsorb on the catalyst. For Fig. S6a, it can be found that some catalysts (Pd-, Os-, Fe-, Rh-, and Ir-C_7N_3) have weak adsorption strength, which may greatly affect the subsequent catalytic process. A similar condition has been observed with other catalysts (*e.g.*, Pd- and Zn-$C_{10}N_3$, Rh-, and Zn-$C_{13}N_3$, Rh-, and Zn-$C_{19}N_3$). Thus, their subsequent NO_3RR activity is not discussed.

Then, the NO_3RR activity on all screened stable catalysts are evaluated and the limiting potentials ($U_L(NO_3RR)$) are calculated, as shown in Fig. 2b. The closer the value of $U_L(NO_3RR)$ is to 0 V, the higher the NO_3RR activity of the catalyst. In other words, the darker the red region, the better the catalytic activity of the catalyst. Obviously, for M_2-C_7N_3, the $U_L(NO_3RR)$ value of Zn_2-C_7N_3 (−0.36 V) is closest to 0 V, which indicates that it has the best catalytic activity in this type of catalyst. Moreover, the $U_L(NO_3RR)$ values of Au_2-$C_{10}N_3$, Fe_2-$C_{13}N_3$, Fe_2-$C_{19}N_3$, and Os_2-$C_{19}N_3$ are

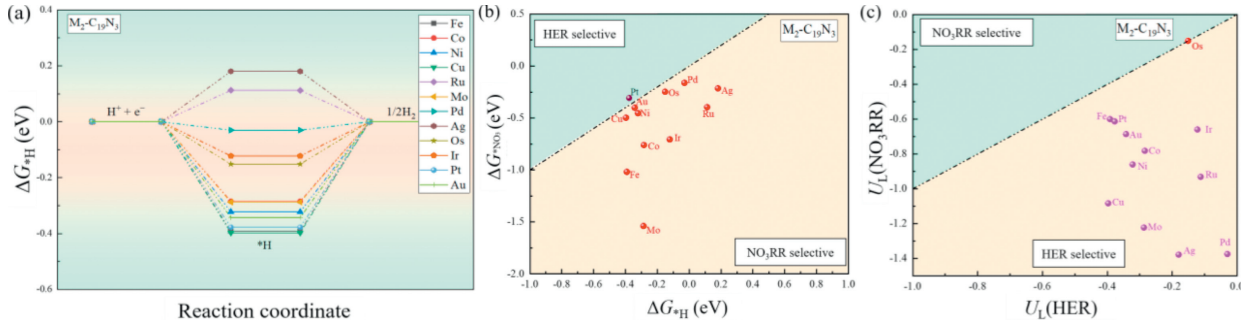


Fig. 3. (a) Free energy diagrams of HER on M_2-$C_{19}N_3$. (b) ΔG_{*H} and ΔG_{*NO_3} values on M_2-$C_{19}N_3$. (c) Limiting potentials for NO_3RR and HER on M_2-$C_{19}N_3$.

between −0.60 V and 0 V, which indicates that they have excellent NO_3RR catalytic activity. Moreover, the formation of $*NO_3H$ and *NOH in the catalytic process of NO_3RR is often accompanied by the input of external energy. Therefore, ΔG_{*NO3H} and ΔG_{*NOH} as activity descriptors with U_L are used to construct the volcano plot, as shown in the Fig. 2c. It can be seen that the darker the red region, the better the catalytic activity, that is, the best NO_3RR catalytic activity of Os_2-$C_{19}N_3$. In particular, by comparing their values with other reported excellent NO_3RR catalysts in Table S1 (Supporting information), such as HOF-Ti1 ($U_L(NO_3RR) = -0.15$ V) [47], V_2-Pc ($U_L(NO_3RR) = -0.25$ V [50], Os/GDY ($U_L(NO_3RR) = -0.37$ V) [13], Os_2-$C_{19}N_3$ has excellent catalytic activity with the $U_L(NO_3RR)$ of −0.15 V. Thus, it can be used as the most promising NO_3RR catalyst.

Since the screened catalysts proved to have good catalytic activity, their catalytic mechanisms are studied in detail. In order to evaluate the reaction pathway on M_2-C_xN_3, the E_{ads} values of *NO are calculated. The more negative the E_{ads} values, the stronger the adsorption of *NO on M_2-C_xN_3. For Zn_2-C_7N_3 in Fig. 2d, *NO is more inclined to take the *NO-end route rather than the *NO-side route, because the adsorption energy (E_{*NO}) on Zn_2-C_7N_3 for *NO-end ($E_{*NO\text{-}end} = -0.53$ eV) is less than that of *NO-side ($E_{*NO\text{-}side} = -0.50$ eV). For the whole reaction process, the potential-determining step (PDS) is determined to be the largest ΔG. Obviously, the PDS is $* + NO_3^- \rightarrow *NO_3$ and the corresponding value is 0.36 eV, which requires additional energy. The similar condition has been reported for $M-N-C$ catalyst [51]. The NO_3RR pathway of Zn_2-C_7N_3 is $* + NO_3^- \rightarrow *NO_3 \rightarrow *NO_3H \rightarrow NO_2 \rightarrow *NO_2H \rightarrow *NO \rightarrow *NOH \rightarrow *N \rightarrow *NH \rightarrow *NH_2 \rightarrow *NH_3 \rightarrow * + NH_3$. For Au_2-$C_{10}N_3$, Fe_2-$C_{13}N_3$, and Fe_2-$C_{19}N_3$ in Fig. S7 (Supporting information), *NO also exists in the form of *NO-end. Thus, the reaction pathway of them and Zn_2-C_7N_3 are the same. Their PDS are *NO, $*NO_3$, and $*NO_3$ hydrogenation, respectively, and the corresponding values are 0.53, 0.58, and 0.60 eV respectively. Moreover, for Os_2-$C_{19}N_3$ in Fig. 2e, $*NO_2$ is hydrogenated to form $*NO_2H$ as the PDS, and the corresponding value is 0.15 eV. Unlike Zn_2-C_7N_3, *NO is more likely to adsorb in the form of *NO-side ($E_{*NO\text{-}side} = -1.90$ eV) than *NO-end ($E_{*NO\text{-}end} = 1.75$ eV), which changes the subsequent hydrogenation pathway. The results show that *NOH is more likely to be hydrogenated to remove H_2O, rather than hydrogenated to produce *NHOH. Thus, the NO_3RR pathway of Os_2-$C_{19}N_3$ is $* + NO_3^- \rightarrow *NO_3 \rightarrow *NO_3H \rightarrow NO_2 \rightarrow *NO_2H \rightarrow *NO \rightarrow *NOH \rightarrow *N \rightarrow *NH \rightarrow *NH_2 \rightarrow *NH_3 \rightarrow * + NH_3$. In summary, different catalysts will produce different configurations of adsorption intermediates, which will affect the adsorption strength of catalyst for reaction intermediates. Then the PDS of the catalyst may be changed, changing the reaction pathway of the catalyst, thus affecting the catalytic activity of the catalyst.

HER is a competitive reaction of NO_3RR, which will affect the reaction efficiency of NO_3RR. Therefore, it is very necessary to evaluate the performance of catalyst for HER. In this paper, two methods are used to evaluate the selectivity of the catalyst and ΔG_{*NO_3}, ΔG_{*H}, $U_L(NO_3RR)$, and U_L(HER) are calculated. The catalyst with more negative ΔG_{*NO_3} value and more positive $U_L(NO_3RR)$ value has better catalytic selectivity. First, ΔG_{*H} values on all screened catalysts are calculated and the free energy diagrams of HER are plotted in Fig. 3a and Figs. S8a-c (Supporting information). Then, the values of ΔG_{*H} and ΔG_{*NO_3} values are compared for preliminary screening of M_2-C_xN_3 with catalytic potential for NO_3RR. The values of ΔG_{*NO_3} should be more negative than that of ΔG_{*H}, indicating that M_2-C_xN_3 preferentially adsorbs NO_3. That is, M_2-C_xN_3 in the yellow region has excellent NO_3RR catalytic selectivity in Fig. 3b and Figs. S8d-f (Supporting information). Obviously, as the number of x increases, more M_2-C_xN_3 have excellent NO_3RR catalytic selectivity. Moreover, U_L is the dominant factor in the entire electrocatalytic process and is more suitable for evaluating the catalytic selectivity of NO_3RR and HER of M_2-C_xN_3. Therefore, to determine that NO_3RR has an energy advantage over HER, $U_L(NO_3RR)$ and U_L(HER) on M_2-C_xN_3 are compared, as shown in Fig. 3c and Figs. S8g-i (Supporting information). M_2-C_xN_3 in the blue region indicates the lower $U_L(NO_3RR)$ values, which means better NO_3RR selectivity. Overall, Os_2-$C_{19}N_3$ has superior catalytic potential for NO_3RR, and the values of $U_L(NO_3RR)$ is −0.15 V. It is worth noting that although the remaining M_2-C_xN_3 do not have excellent NO_3RR catalytic selectivity, their HER activity is extremely valuable. Rh_2-$C_{10}N_3$, Os_2-$C_{13}N_3$, and Pd_2-$C_{19}N_3$ possess excellent HER catalytic activity, the corresponding U_L(HER) values are −0.02, −0.05, and −0.03 V, which is far superior to other reported excellent HER catalysts in Table S2 (Supporting information), such as, Rh-2D-SA (U_L(HER) = −0.13 V) [46], *Sc*@C_3–CN (U_L(HER) = −0.07 V) [52], Ti@Corrole (U_L(HER) = −0.02 V) [53], and Au@BC_3 (U_L(HER) = −0.04 V) [54]. After a series of screening strategies in Fig. S9 (Supporting information), 52 stable catalysts are selected. On this basis, the adsorption behavior of NO_3, catalytic activity of NO_3RR and competitive reaction HER are investigated. Finally, Os_2-$C_{19}N_3$ with the best NO_3RR catalytic activity is selected.

According to the above calculation results of $U_L(NO_3RR)$, Os_2-$C_{19}N_3$ has the best catalytic activity of NO_3RR ($U_L(NO_3RR) = -0.15$ V). Therefore, the detailed electronic structure analysis of Os_2-$C_{19}N_3$ is carried out. Firstly, Os_2-$C_{19}N_3$ and reaction species are divided into two moieties respectively. That is, Os_2-$C_{19}N_3$ is moiety-1 and the reaction species is moiety-2, as shown in Fig. S10a (Supporting information). Then, the Mulliken charge is calculated and charge variation during the process of NO_3RR on Os_2-$C_{19}N_3$ is analyzed in Fig. S10b (Supporting information). Obviously, it can be observed that there is a significant charge transfer between Os_2-$C_{19}N_3$ and reaction species, which indicates a strong interaction between them. In addition, the amount of charge transfer between different reaction species and the catalyst is different, which

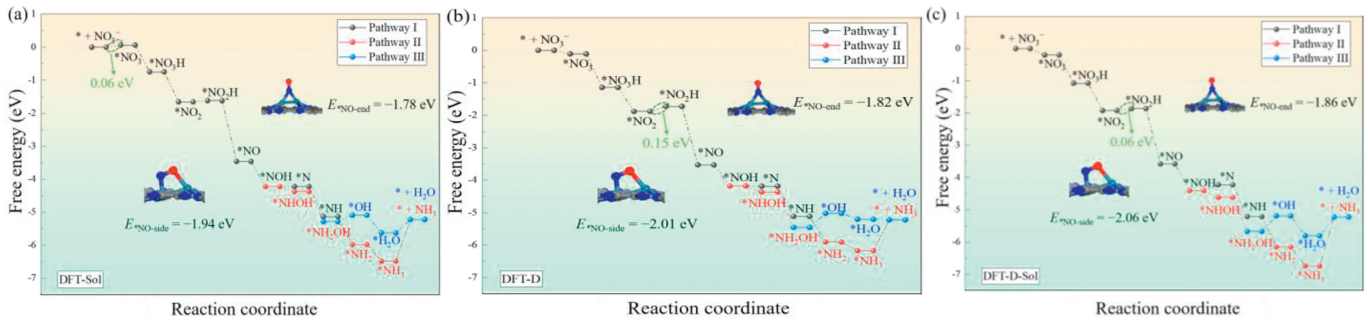


Fig. 4. Free energy diagrams for NO_3RR under the conditions of (a) DFT-Sol, (b) DFT-D, and (c) DFT-D-Sol for $Os_2\text{-}C_{19}N_3$.

will affect the interaction between the reaction species and the $Os_2\text{-}C_{19}N_3$. This can change the adsorption strength of $Os_2\text{-}C_{19}N_3$ towards reaction species, thereby altering their catalytic activity. In order to more clearly show the interaction between $Os_2\text{-}C_{19}N_3$ and reaction species, deformation charge density of reaction species on $Os_2\text{-}C_{19}N_3$ are calculated and displayed in Fig. S11 (Supporting information). The blue and yellow represent electron accumulation and depletion, respectively. It can be observed that there is obvious accumulation and depletion between $Os_2\text{-}C_{19}N_3$ and reaction species. This further indicates that there is a strong interaction between $Os_2\text{-}C_{19}N_3$ and reaction species during NO_3RR process, which is consistent with the above studies.

Finally, in order to further investigate the stability of $Os_2\text{-}C_{19}N_3$ at different temperatures (300 and 500 K), FPMD is calculated and exhibited in Fig. S12 (Supporting information). The results of FPMD calculation show that the energy always oscillates at the equilibrium state regardless of 300 or 500 K, which indicates that $Os_2\text{-}C_{19}N_3$ can exist stably at 300 and 500 K. This calculation results further verify the excellent stability of $Os_2\text{-}C_{19}N_3$.

It is well known that solvation effects (DFT-Sol) and dispersion corrections (DFT-D) will enhance the adsorption strength of the reaction intermediates on catalyst to a certain extent. In addition, it is extremely important to evaluate the catalytic activity of $Os_2\text{-}C_{19}N_3$ under the conditions of DFT-Sol, DFT-D, and DFT-D-Sol. Therefore, a detailed study is conducted on the catalytic process of $Os_2\text{-}C_{19}N_3$ towards NO_3RR under the conditions of solvation effects and dispersion corrections. The free energy diagrams are plotted in Fig. 4. First, under the condition of solvation in Fig. 4a, the adsorption strength of *NO on of $Os_2\text{-}C_{19}N_3$ is enhanced, which are −1.78 ($E_{*NO\text{-}end}$) and −1.94 eV ($E_{*NO\text{-}side}$). Then, it is found that when $Os_2\text{-}C_{19}N_3$ adsorbs *NOH for further hydrogenation, $Os_2\text{-}C_{19}N_3$ is more inclined to form *NHOH than *N. It is speculated that the solvation effects on *NHOH of $Os_2\text{-}C_{19}N_3$ is greater than that on *N. That is, the NO_3RR of $Os_2\text{-}C_{19}N_3$ is carried out in pathway II. In particular, when the $Os_2\text{-}C_{19}N_3$ adsorbs $*NH_2OH$, $Os_2\text{-}C_{19}N_3$ can form *OH by hydrogenation to remove NH_3 (pathway III), and can also form $*NH_2$ by hydrogenation to remove H_2O (pathway II). It can be found that $*NH_2OH$ to *OH requires the input of additional energy, which is disadvantageous. Thus, $*NH_2OH$ is more inclined to hydrogenate to form $*NH_2$. In summary, under DFT-Sol, the optimal reaction pathway of the catalyst is pathway II, that is, $* + NO_3^- \rightarrow *NO_3 \rightarrow *NO_3H \rightarrow NO_2 \rightarrow *NO_2H \rightarrow *NO \rightarrow *NOH \rightarrow *NHOH \rightarrow *NH_2OH \rightarrow *NH_2 \rightarrow *NH_3 \rightarrow * + NH_3$. Similarly, under the conditions of DFT-D and DFT-D-Sol, the optimal pathway for $Os_2\text{-}C_{19}N_3$ to catalyze NO_3RR are also pathway II, as shown in Figs. 4b and c. It can be found that under the three conditions, $Os_2\text{-}C_{19}N_3$ still possesses excellent catalytic activity, and the $U_L(NO_3RR)$ values are −0.06, −0.15, and −0.06 V, respectively. In summary, solvation effects and dispersion corrections can change the adsorption behavior of reaction intermediates on $Os_2\text{-}C_{19}N_3$, thereby regulating the NO_3RR catalytic activity of $Os_2\text{-}C_{19}N_3$.

In summary, this work is aim to search for highly active NO_3RR electrocatalysts through efficient screening strategy by DFT method. The four-step screening strategy was used to search for high-performance NO_3RR electrocatalysts. Firstly, for this screening strategy, structural stability is evaluated by calculating E_f and U_{diss}. The results show that different transition metal doped will preferentially generate different catalyst configurations. Then, the results of DOS provide strong evidence for the stability of the catalyst and the band structure, which makes it possible for $M_2\text{-}C_xN_3$ to electrocatalyze NO_3RR. Secondly, the adsorption behaviors of NO_3 as a prerequisite step for NO_3RR, the adsorption configuration is considered. Thirdly, the electrocatalyst with excellent NO_3RR is found by calculating $U_L(NO_3RR)$. Different $M_2\text{-}C_xN_3$ will produce different configurations of adsorption intermediates, which will affect the adsorption strength of $M_2\text{-}C_xN_3$ for the intermediates, and thus affect the catalytic activity of $M_2\text{-}C_xN_3$. $Au_2\text{-}C_{10}N_3$, $Fe_2\text{-}C_{13}N_3$ $Fe_2\text{-}C_{19}N_3$, and $Os_2\text{-}C_{19}N_3$ possess lower $U_L(NO_3RR)$ values with −0.53, −0.58, −0.60, and −0.15 V, respectively. In particular, the free energy diagrams of $M_2\text{-}C_xN_3$ with excellent NO_3RR catalytic performance have been studied. The NO_3RR process of $Os_2\text{-}C_{19}N_3$ is $* + NO_3^- \rightarrow *NO_3 \rightarrow *NO_3H \rightarrow NO_2 \rightarrow *NO_2H \rightarrow *NO \rightarrow *NOH \rightarrow *N \rightarrow *NH \rightarrow *NH_2 \rightarrow *NH_3 \rightarrow * + NH_3$. In addition, applying the $\Delta G_{*NO_3} < \Delta G_{*H}$ as evaluation criteria, the results show that as the number of x increases, more $M_2\text{-}C_xN_3$ have excellent NO_3RR catalytic selectivity. The applying $U_L(NO_3RR) < U_L(HER)$ as evaluation criteria, $Os_2\text{-}C_{19}N_3$ has superior catalytic potential for NO_3RR, and the values of $U_L(NO_3RR)$ is −0.15 V. The volcano plot also proves that $Os_2\text{-}C_{19}N_3$ possesses the best NO_3RR catalytic activity. It is worth noting that $Rh_2\text{-}C_{10}N_3$, $Os_2\text{-}C_{13}N_3$, and $Pd_2\text{-}C_{19}N_3$ possess excellent HER catalytic activity, the corresponding $U_L(HER)$ values are −0.02, −0.05, and −0.03 V. In particular, it can be found that under the conditions of DFT-Sol, DFT-D, and DFT-D-Sol, $Os_2\text{-}C_{19}N_3$ still possesses excellent catalytic activity, and the $U_L(NO_3RR)$ values are −0.06, −0.15, and −0.06 V, respectively. For electronic structure analysis and stability of $Os_2\text{-}C_{19}N_3$ (the best NO_3RR performance), the Mulliken charge is calculated and charge variation during the process of NO_3RR is analyzed. Different amounts of charge transfer can change the adsorption strength of $Os_2\text{-}C_{19}N_3$ towards reaction species, thereby altering their catalytic activity. This conclusion is further proved by the deformation charge density. Finally, the results of FPMD calculation show that $Os_2\text{-}C_{19}N_3$ can exist stably at 300 and 500 K. Thus, $Os_2\text{-}C_{19}N_3$ shows excellent thermodynamic and electrochemical stability by calculating E_f and U_{diss}, and also possesses low $U_L(NO_3RR)$ values, which is a NO_3RR catalyst with high catalytic potential. This work can provide a possible reference value for further exploration of novel NO_3RR catalysts and ammonia synthesis.

Declaration of competing interest

The authors declare that they have no known competing financial interests or personal relationships that could have appeared to influence the work reported in this paper.

CRediT authorship contribution statement

Yahui Li: Investigation, Writing – original draft, Formal analysis. **Quanchen Feng:** Writing – review & editing. **Krisztina László:** Writing – review & editing. **Ying Wang:** Methodology, Software, Writing – review & editing, Conceptualization, Funding acquisition.

Acknowledgments

This work was supported by National Natural Science Foundation of China (NSFC, No. 22276138), Science & Technology Commission of Shanghai Municipality (No. 22230712800), and the Fundamental Research Funds for the Central Universities and the Foundation of State Key Laboratory of Pollution Control and Resource Reuse (Tongji University) (No. 2022-4-ZD-07). We acknowledge the National Supercomputing Center in Shenzhen for providing the computational resources and Materials Studio.

Supplementary materials

Supplementary material associated with this article can be found, in the online version, at doi:10.1016/j.cclet.2025.111536.

References

[1] Y. Chen, C. Chen, Y. Liu, et al., Chin. Chem. Lett. 34 (2023) 108489.
[2] A. Kalair, N. Abas, M.S. Saleem, et al., Energy Storage 3 (2021) 1–27.
[3] L. Fang, S. Wang, S. Lu, et al., Chin. Chem. Lett. 35 (2024) 108864.
[4] X. Yang, S. Mukherjee, T. O'Carroll, et al., Angew. Chem. Int. Ed. 62 (2023) e202215938.
[5] X. Li, S. Lyu, X. Lang, Environ. Res. 195 (2021) 110851.
[6] X. Wang, S. Zhang, X. Li, et al., J. Mater. Chem. A 9 (2021) 16405–16410.
[7] T. Feng, F. Li, X. Hu, et al., Chin. Chem. Lett. 34 (2023) 107862.
[8] M.A. Nawaz, R. Blay-Roger, M. Saif, et al., ACS Catal. 13 (2023) 14415–14453.
[9] C. Smith, A.K. Hill, L. Torrente-Murciano, Energy Environ. Sci. 13 (2020) 331–344.
[10] M. Wang, M.A. Khan, I. Mohsin, et al., Energy Environ. Sci. 14 (2021) 2535–2548.
[11] A. Liu, Y. Yang, D. Kong, et al., Appl. Surf. Sci. 536 (2021) 147851.
[12] C.H. Lee, S. Pahari, N. Sitapure, et al., ACS Catal. 12 (2022) 15609–15617.
[13] M. Yang, Z. Wang, D. Jiao, et al., Appl. Surf. Sci. 592 (2022) 153213.
[14] Y. Wang, D. Wu, P. Lv, et al., Nanoscale 14 (2022) 10862–10872.
[15] R. Zhu, Y. Qin, T. Wu, et al., Small 20 (2024) 1–9.
[16] P. Lv, D. Wu, B. He, et al., J. Mater. Chem. A 10 (2022) 9707–9716.
[17] Z. Wu, Y. Song, H. Guo, et al., Interdiscip. Mater. 3 (2024) 245–269.
[18] Z. Wu, X. Kang, S. Wang, et al., Adv. Funct. Mater. 34 (2024) 2406917.
[19] H. Niu, Z. Zhang, X. Wang, et al., Adv. Funct. Mater. 31 (2021) 2008533.
[20] E. Murphy, Y. Liu, I. Matanovic, et al., ACS Catal. 12 (2022) 6651–6662.
[21] J. Xu, J. Mahmood, Y. Dou, et al., Adv. Mater. 29 (2017) 1702007.
[22] D. Li, A. Zhang, Z. Feng, et al., ACS Appl. Mater. Interfaces 16 (2024) 5779–5791.
[23] P. Hou, Y. Huang, F. Ma, et al., Appl. Surf. Sci. 599 (2022) 153880.
[24] C. Chen, M. Sun, K. Wang, Y. Li, SmartMat 3 (2022) 533–564.
[25] F. Besharat, F. Ahmadpoor, Z. Nezafat, et al., ACS Catal. 12 (2022) 5605–5660.
[26] S. Zhu, M.X. Qin, L. Chen, et al., J. Phys. Chem. Lett. 14 (2023) 4185–4191.
[27] L. Lv, Y. Shen, J. Liu, et al., J. Phys. Chem. Lett. 12 (2021) 11143–11150.
[28] L. Wu, T. Guo, T. Li, Adv. Funct. Mater. 32 (2022) 203439.
[29] Z. Lv, L. Zhao, S. Zhou, et al., Appl. Catal. B: Environ. 351 (2024) 124003.
[30] H. Han, J. Im, M. Lee, et al., Appl. Catal. B: Environ. 320 (2023) 121953.
[31] D. Wu, K. Chen, P. Lv, et al., Nano Lett. 24 (2024) 8502–8509.
[32] N. Sathishkumar, H.T. Chen, J. Phys. Chem. C 127 (2023) 994–1005.
[33] L. Lv, Y. Shen, M. Zhou, et al., J. Mater. Chem. A 12 (2024) 6733–6746.
[34] R. Tan, Z. Li, P. Zhou, et al., J. Phys. Chem. C 125 (2021) 6082–6089.
[35] Y. Li, Y. Feng, D. Zheng, et al., Chem. Eng. J. 476 (2023) 146753.
[36] X. Cai, L. Luo, X. Zhao, et al., Mol. Catal. 554 (2024) 113844.
[37] B. Delley, J. Chem. Phys. 92 (1990) 508–517.
[38] B. Delley, J. Chem. Phys. 113 (2000) 7756–7764.
[39] J.P. Perdew, J.A. Chevary, S.H. Vosko, et al., Phys. Rev. B 48 (1993) 4978.
[40] J.P. Perdew, K. Burke, M. Ernzerhof, Phys. Rev. Lett. 77 (1996) 3865–3868.
[41] J. Greeley, J.K. Nørskov, Electrochim. Acta 52 (2007) 5829–5836.
[42] X. Guo, J. Gu, S. Lin, et al., J. Am. Chem. Soc. 142 (2020) 5709–5721.
[43] X. Lu, H. Song, J. Cai, et al., Electrochem. Commun. 129 (2021) 107094.
[44] A.A. Peterson, F. Abild-Pedersen, F. Studt, et al., Energy Environ. Sci. 3 (2010) 1311–1315.
[45] J.K. Nørskov, J. Rossmeisl, A. Logadottir, et al., J. Phys. Chem. B 108 (2004) 17886–17892.
[46] X. Chen, Y. Li, X. Zhao, Surf. Interfaces. 38 (2023) 102821.
[47] S. Wang, Y. Wang, Y. Fu, et al., J. Energy Chem. 87 (2023) 408–415.
[48] D. Liu, L. Qiao, S. Peng, et al., Adv. Funct. Mater. 33 (2023) 2303480.
[49] P. Xue, X. Zhao, D. Zheng, et al., Comput. Mater. Sci. 234 (2024) 112778.
[50] F. Rehman, S. Kwon, C.B. Musgrave, et al., Nano Energy 103 (2022) 107866.
[51] Y. Wang, M. Shao, ACS Catal. 12 (2022) 5407–5415.
[52] Y. Yang, X. Zhao, T. Liu, et al., Int. J. Hydrogen Energy 56 (2024) 949–958.
[53] F. Yaseen, M.A. Hashmi, Q.U. Ain, et al., Int. J. Hydrogen Energy 57 (2024) 1389–1397.
[54] L. Pan, X. Kang, S. Gao, et al., Phys. Chem. Chem. Phys. 26 (2023) 1011–1016.